Local wind regime induced by giant linear dunes — Supplementary Material —

C. Gadal* · **P. Delorme** · **C. Narteau** · **G.F.S. Wiggs** · **M. Baddock** · **J.M. Nield** · **P. Claudin**

* Institut de Mécanique des Fluides de Toulouse, Université de Toulouse Paul Sabatier, CNRS, Toulouse INP-ENSEEIHT, Toulouse, France.
cyril.gadal@imft.fr

1. Shear velocity and calibration of the hydrodynamical roughness

As the regionally predicted and locally measured velocities are available at different heights, we can not compare them directly. We therefore convert all velocities into shear velocities u_*, characteristic the turbulent logarithmic velocity profile (Spalding 1961; Stull 1988):

$$\frac{u(z)}{u_*} = \frac{1}{\kappa} \ln\left(\frac{z}{z_0}\right), \tag{15}$$

where z is the vertical coordinate, $\kappa = 0.4$ the von Kármán constant and z_0 the hydrodynamic roughness. Note that, strickly speaking, this logarithmic profile is valid for a neutrally stratified ABL only. Vertical density gradients occuring in other conditions may thus induce large discrepancies (Monin and Obukhov 1954; Garratt 1994; Dyer 1974). However, as our wind measurements are in the flow region close enough to the surface, where these effects are negligible, this logarithmic wind profile remains a farily good approximation in all conditions (Gunn et al. 2021). Several measurements of hydrodynamic roughnesses are available (Raupach 1992; Bauer et al. 1992; Brown et al. 2008; Nield et al. 2014). In the absence of sediment transport, it is governed by the geometric features of the bed (Flack and Schultz 2010; Pelletier and Field 2016). When aeolian saltation occurs, it is rather controlled by the altitude of Bagnold's focal point (Durán et al. 2011; Valance et al. 2015), which depends on the wind velocity and grain properties (Sherman and Farrell 2008; Zhang et al. 2016; Field and Pelletier 2018). Whether associated with geometric features or with sediment transport, its typical order of magnitude is the millimetre scale on sandy surfaces.

We do not have precise velocity vertical profiles to be able to deduce an accurate value of z_0 in the various environments of the meteorological stations (vegetated, arid, sandy). Our approach is to rather select the hydrodynamic roughness which allows for the best possible matching between the regionally predicted and locally measured winds, i.e. minimising the relative difference δ between the wind vectors of both datasets:

$$\delta = \frac{\sqrt{\langle \|\boldsymbol{u}_{*,\mathrm{era}} - \boldsymbol{u}_{*,\mathrm{station}}\|^2 \rangle}}{\sqrt{\langle \|\boldsymbol{u}_{*,\mathrm{era}}\| \rangle \langle \|\boldsymbol{u}_{*,\mathrm{station}}\| \rangle}}, \tag{16}$$

where $\langle . \rangle$ denotes time average. This parameter is computed for values of z_0 in ERA5-Land analysis ranging from 10^{-5} m to 10^{-2} m for the four different stations. Note that for the North Sand Sea and South Sand Sea stations, where the giant dunes feedback presumably affect the wind, we take into account the non-deflected winds only in the calculation of δ (with a 15° tolerance).

As shown in Online Resource Fig. S3, the minimum values of δ in the space $(z_0^{\mathrm{ERA5Land}}, z_0^{\mathrm{local}})$ form a line. We thus set the roughness in the ERA5-Land analysis to the typical value $z_0 = 10^{-3}$ m, and deduce the corresponding ones for the local stations. It leads to 2.7, 0.8, 0.1 and 0.5 mm for the Etosha West, North Sand Sea, Huab and South Sand Sea stations, respectively. Importantly, this approach somewhat impacts the calculation of the shear velocities, but not that of the wind directions. As such, most of our conclusions are independent of such a choice. However, it may affect the magnitude of the wind velocity attenuation/amplification in flow confinement situations.

2. Computation of the ABL characteristics

The estimation of the non-dimensional numbers associated with the ABL requires the computation of representative meteorological quantities. In arid areas, the vertical structure of the atmosphere can be approximated by a well mixed convective boundary layer of height H, topped by the stratified free atmosphere (Stull 1988; Shao 2008). In this context, one usually introduces the virtual potential temperature T_{vp}, which is a constant T_0 inside the boundary layer, and increases linearly in the FA (Online Resource Fig. S8a):

$$T_{\mathrm{vp}}(z) = \begin{cases} T_0 & \text{for } z \leq H, \\ T_0 \left(1 + \dfrac{\Delta T_{\mathrm{vp}}}{T_0} + \dfrac{N^2}{g}(z - H)\right) & \text{for } z \geq H, \end{cases} \tag{17}$$

where ΔT_{vp} is the temperature discontinuity at the capping layer and $N = \sqrt{g \partial_z T_{\mathrm{vp}}/T_0}$ is the Brunt-Väisälä frequency, characteristic of the stratification. Note that, under the usual Boussinesq approximation, temperature and air density variations are simply related by $\delta T_{\mathrm{vp}}/T_0 \simeq -\delta\rho/\rho_0$ (see Online Resource of Andreotti et al. (2009)), so that N can equivalently be defined from the density gradient as next to (1).

The ERA5 dataset provides vertical profiles of the geopotential ϕ, the actual temperature T and the specific humidity η at given pressure levels P. The vertical coordinate is then calculated as:

$$z = \frac{\phi R_{\mathrm{t}}}{g R_{\mathrm{t}} - \phi}, \tag{18}$$

where $R_{\mathrm{t}} = 6371229$ m is the reference Earth radius and $g = 9.81$ m s^{-2} is the gravitational acceleration. One also computes the virtual potential temperature as:

$$T_{\mathrm{vp}} = T \left[1 + \left(\frac{M_d}{M_w} - 1\right)\eta\right] \left(\frac{P_0}{P}\right)^{R/C_p}, \tag{19}$$

where $P_0 = 10^5$ Pa is the standard pressure, $R = 8.31$ J/K is the ideal gas constant, $C_p \simeq 29.1$ J/K is the air molar heat capacity, and $M_w = 0.018$ kg/Mol and $M_d = 0.029$ kg/Mol are the molecular masses of water and dry air respectively. The specific humidity is related to the vapour pressure p_w as

$$\eta = \frac{\frac{M_w}{M_d} p_w}{p - \left(1 - \frac{M_w}{M_d}\right) p_w} \,. \tag{20}$$

The ERA5 dataset also provides an estimate of the ABL depth H, based on the behaviour of the Richardson vertical profile. This dimensionless number is defined as the ratio of buoyancy and flow shear terms, and can be expressed as $\mathrm{Ri} = N^2/(\partial_z u)^2$. It vanishes in the lower well-mixed layer where T_{vp} is constant, and increases in the stratified FA. Following the method and calibration of Vogelezang and Holtslag (1996); Seidel et al. (2012), the value $\mathrm{Ri}(z) \simeq 0.25$ has been shown to be a good empirical criterion to give $z \simeq H$ within a precision varying from 50% for the shallower ABL (e.g. at night) to 20% for situations of stronger convection.

Examples of vertical virtual potential temperature profiles deduced from ERA5 are shown in Online Resource Fig. S8a. For each of them, an average temperature is computed below the ABL depth ($z < H$), and a linear function is fitted above, allowing us to extract the temperature jump ΔT_{vp}. Importantly, some profiles display a vertical structure that cannot be approximated by the simple form (17) used here (Online Resource Fig. S8b). In practice, we removed from the analysis all of those leading to the unphysical case $\Delta T_{\mathrm{vp}} < 0$. We have noticed that these 'ill-processed' profiles dominantly occur in winter and are evenly spread across the hours of the day. Importantly, they represent $\simeq 12\%$ of the data only (Online Resource Fig. S8c,d), and we are thus confident that this data treatment does not affect our conclusions.

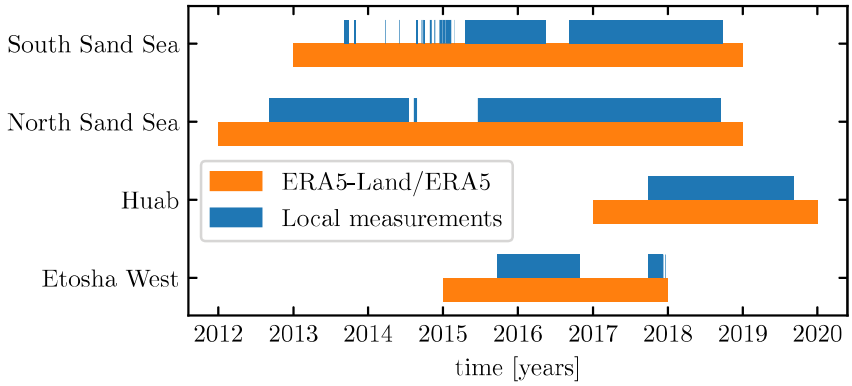

Fig. S1 Gantt chart representing the valid time steps for the two data sets, for all stations.

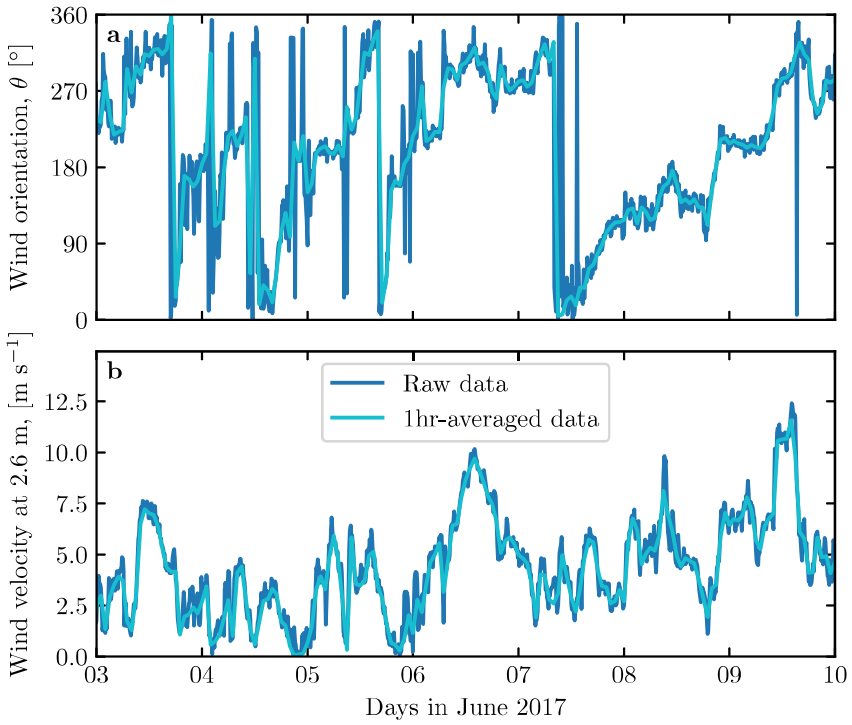

Fig. S2 Local wind measurements: comparison between raw (blue) and hourly-averaged (light blue) data from South Sand Sea station. **a**: wind direction. **b**: wind velocity at height 2.6 m.

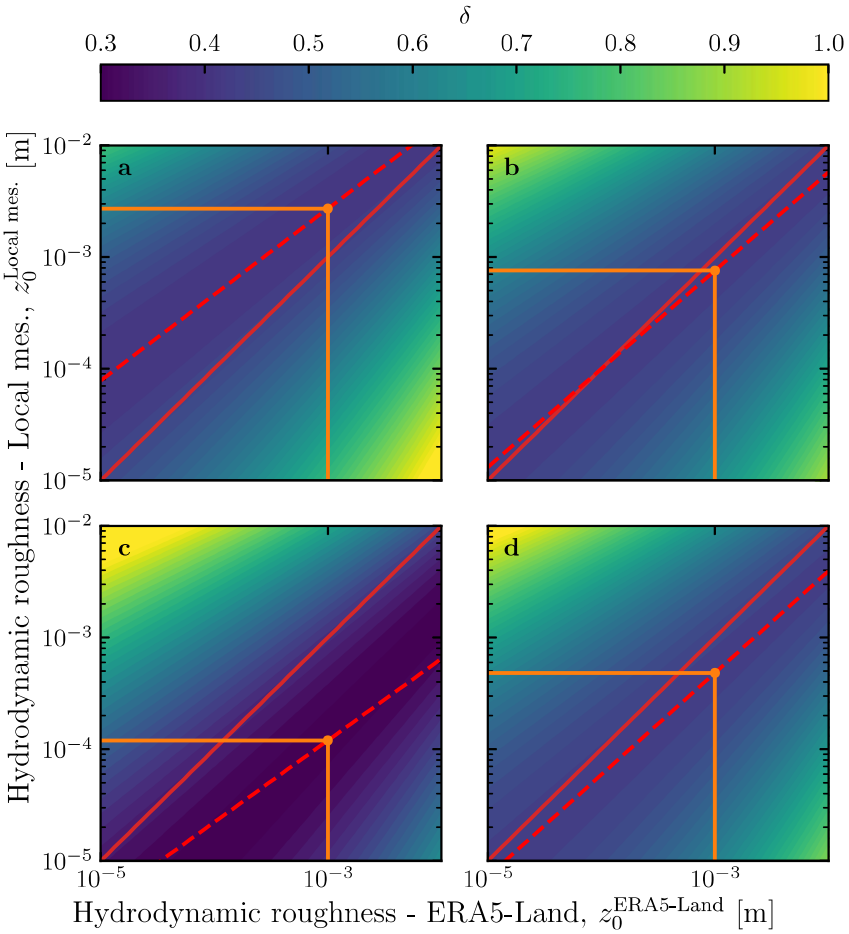

Fig. S3 Calibration of hydrodynamic roughness. The parameter δ (16) quantifying the difference between local and predicted winds is shown in color scale as a function of the hydrodynamic roughnesses chosen for the ERA5-Land and for local winds, for the (**a**) Etosha West, (**b**) North Sand Sea, (**c**) Huab and (**d**) South Sand Sea stations. The red dashed and plain lines shows the minima of δ and the identity line, respectively. The orange lines and dots highlight the chosen hydrodynamic roughnesses for the local winds deduced from setting $z_0^{\text{ERA5-Land}} = 1$ mm.

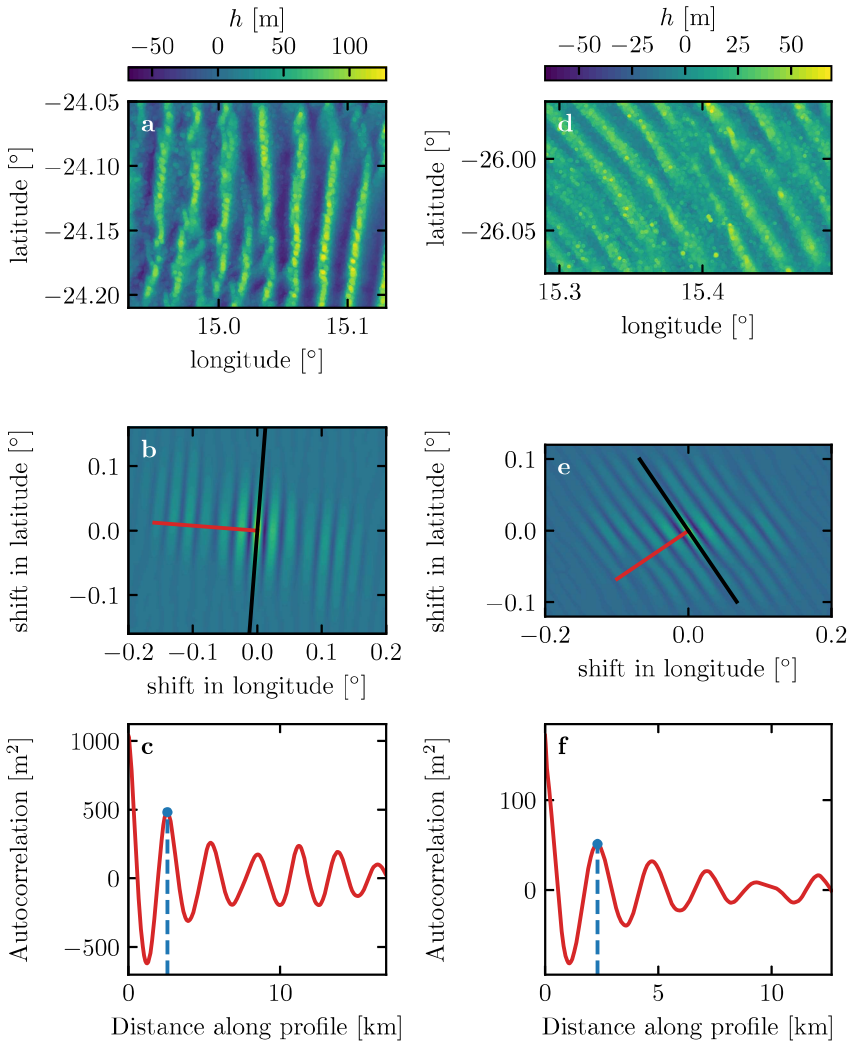

Fig. S4 Analysis of the DEMs of the North Sand Sea (left column – panels **a**, **b**, **c**) and South Sand Sea (right column – panels **d**, **e**, **f**) stations. **a–d**: Bed elevation detrended by a fitted second order polynomial base-line. **b–e**: Autocorrelation matrix shown in color scale. The black line shows the detected dune orientation, and the red line represents the autocorrelation profile along which the dune wavelength is calculated, displayed in **c–f**. The blue lines and dots show the first peak of the autocorrelation profile, whose abscissa gives the characteristic wavelength of the dune pattern.

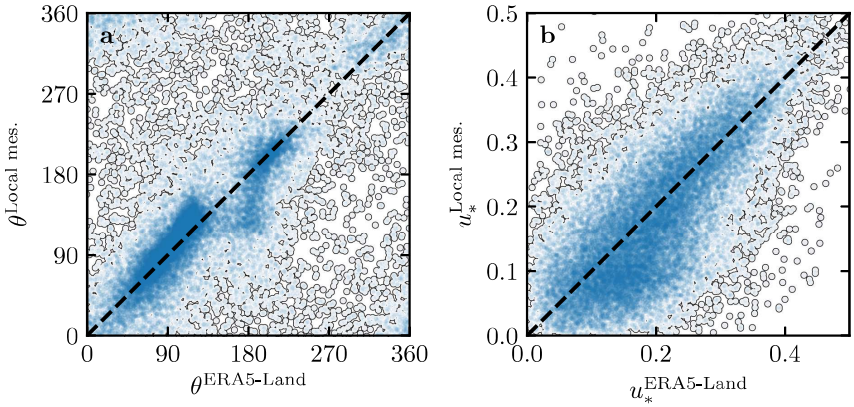

Fig. S5 Statistical comparison of the wind orientation (**a**) and velocity (**b**) between the ERA5-Land dataset and the local measurements for the Huab and Etosha West stations. Data point clustering around identity lines (dashed and black) provide evidence for agreement of the two sets.

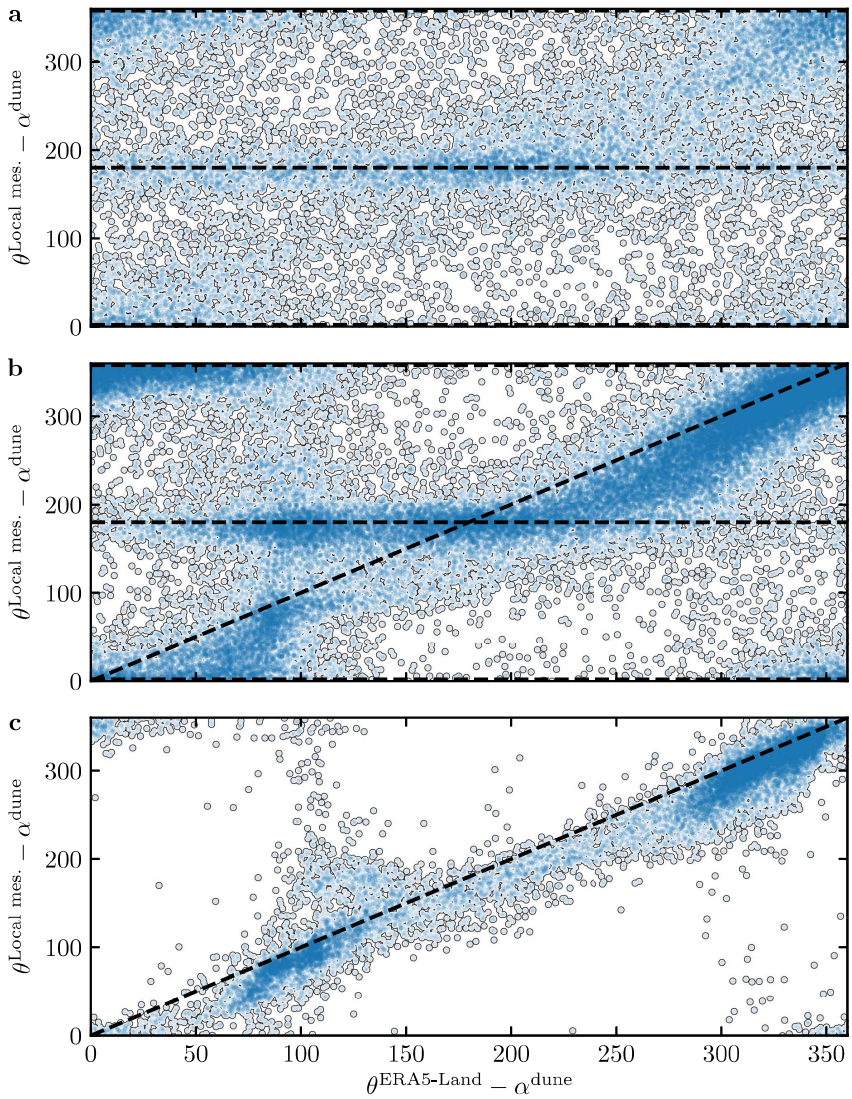

Fig. S6 Statistical comparison of the wind orientation between the ERA5-Land dataset and the local measurements for the South Sand Sea and North Sand Sea stations, for different velocity ranges. **a**: $u_*^{\text{ERA5-Land}} < 0.1$ m s^{-1}. **b**: $0.1 < u_*^{\text{ERA5-Land}} \leq 0.25$ m s^{-1}. **c**: $u_*^{\text{ERA5-Land}} \geq 0.25$ m s^{-1}. The measured dune orientations are subtracted to the wind orientation, which allows us to plot both stations on the same graph. Black dashed lines indicate locally measured orientations aligned with the dune crests (here 0°, 180° and 360° – panels **a**, **b**), as well as the identity lines (panels **b**, **c**).

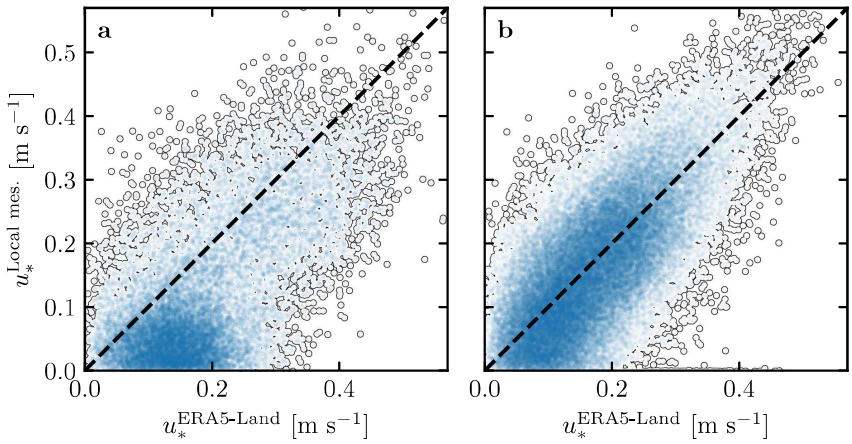

Fig. S7 Statistical comparison of the wind velocity between the ERA5-Land dataset and the local measurements for the South Sand Sea and North Sand Sea stations. **a**: Nocturnal summer easterly wind. **b**: Diurnal southerly wind. Black dashed lines are identity lines. The angle ranges used to select diurnal and nocturnal summer winds are the same as those in Figs. 4 and Figs. 6 of the main article.

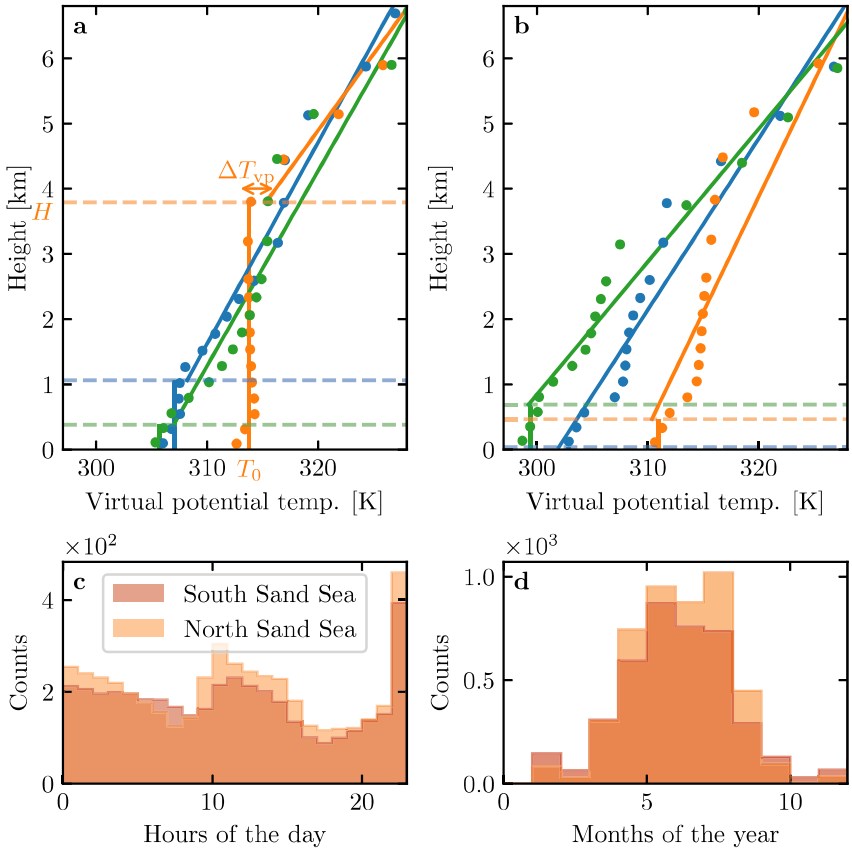

Fig. S8 a: Vertical profiles of the virtual potential temperature at three different times (blue: 29/11/2012 - 11.00 UTC, orange: 21/03/2017 - 12.00 UTC, green: 21/03/2017 - 20.00 UTC) at the South Sand Sea station. Dots: data from the ERA5 reanalysis. Dashed lines: boundary layer height given by the ERA5 reanalysis. Plain lines: vertical (ABL) and linear (FA) fits to estimate the quantities displayed in Online Resource Fig. S9. **b**: Examples of ill-processed vertical profiles at three different times (blue: 2/12/2013 - 23.00 UTC, orange: 20/03/2017 - 00.00 UTC, green: 14/07/2017 - 14.00 UTC) at the South Sand Sea station. Distribution of ill-processed vertical profiles at South (orange) and North (light orange) Sand Sea station: hourly (**c**) and monthly (**d**) counts.

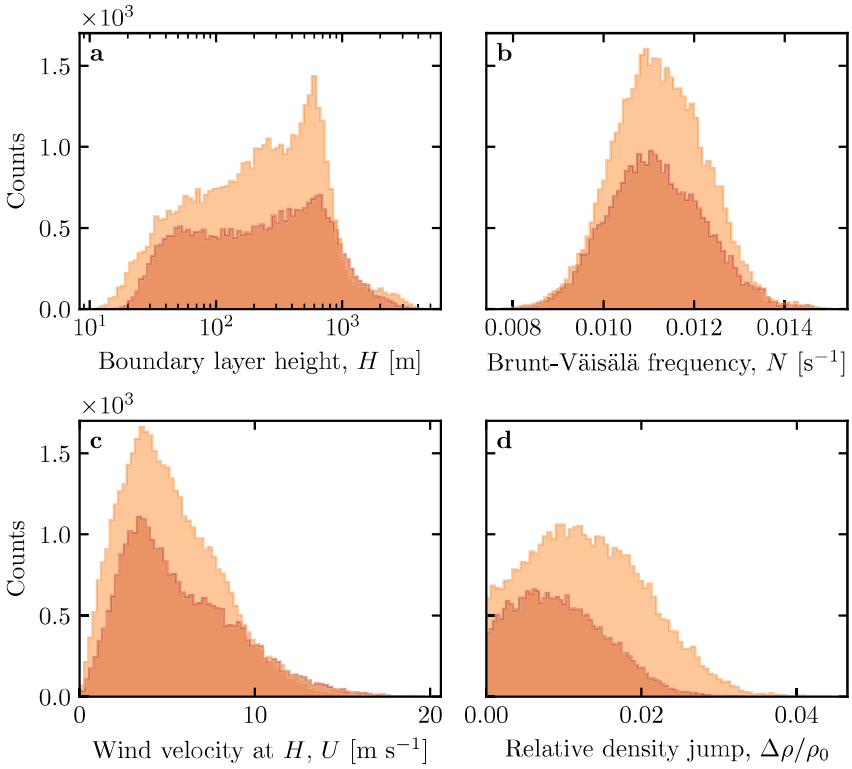

Fig. S9 Distributions of the meteorological parameters resulting from the processing of the ERA5-Land data for the South Sand Sea (orange) and the North Sand Sea (light orange) stations.

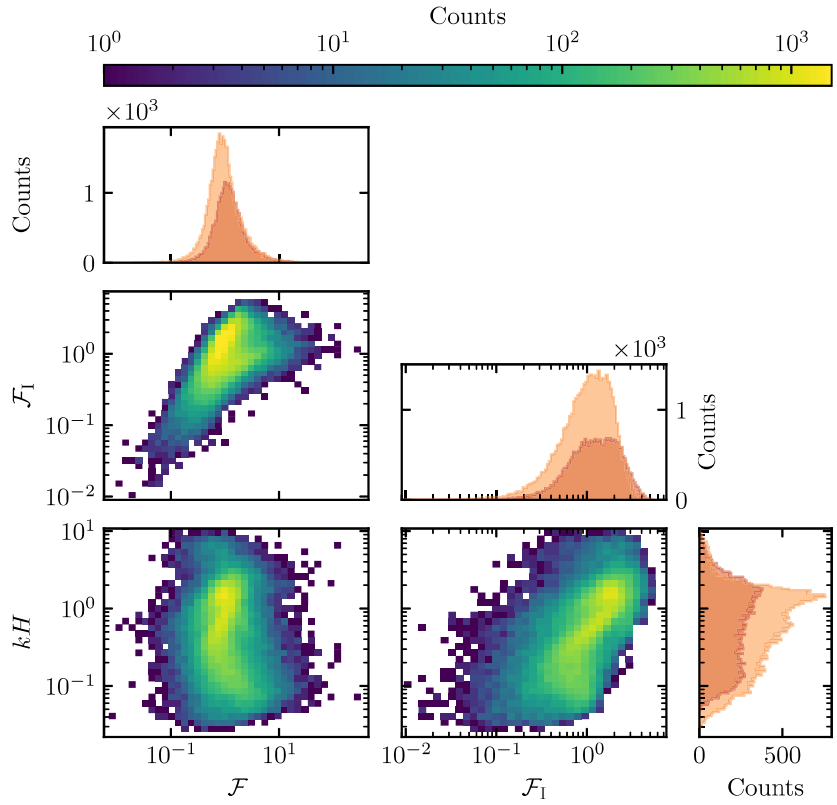

Fig. S10 Non-dimensional parameters distributions. For the marginal distributions, the light orange corresponds to the South Sand Sea station, and the orange to the North Sand Sea station.

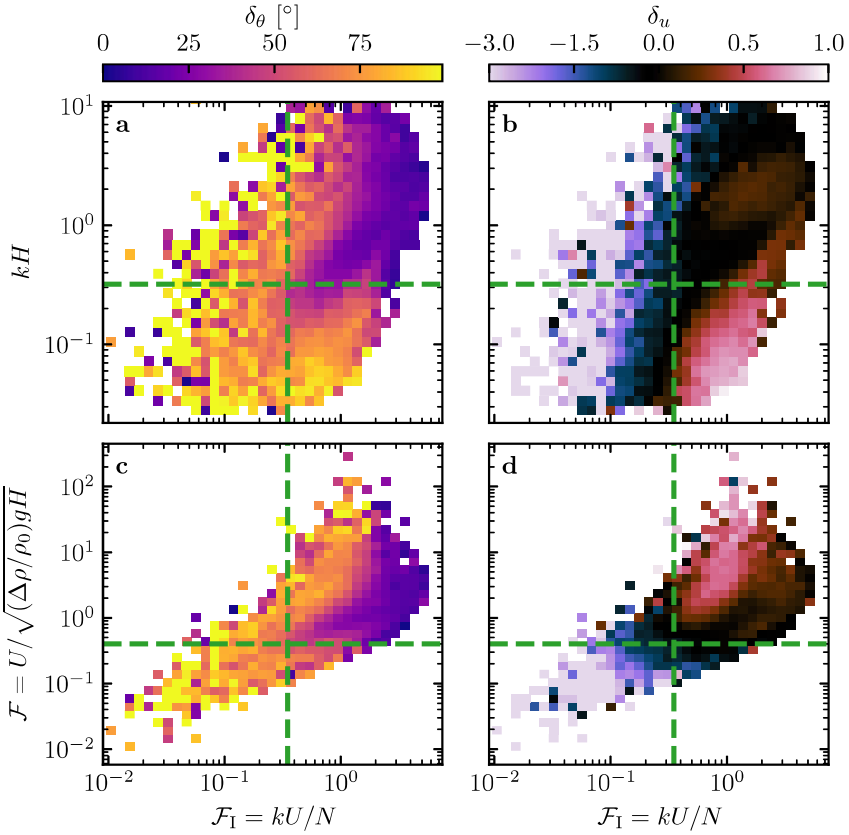

Fig. S11 Regime diagrams of the wind deviation δ_θ and relative attenuation/amplification δ_u in the spaces ($\mathcal{F}_\mathrm{I}$, kH) and ($\mathcal{F}_\mathrm{I}$, $\mathcal{F}$), containing the data from both the North Sand Sea and South Sand Sea stations. Green dashed lines empirically delimit the different regimes. The point density in each bin of the diagrams is shown in Online Resource Fig. S10 – 95% of the data occur in the range $-1 < \delta u < 1$. The similar regime diagrams in the space ($\mathcal{F}$, kH) are shown in Fig. 8.

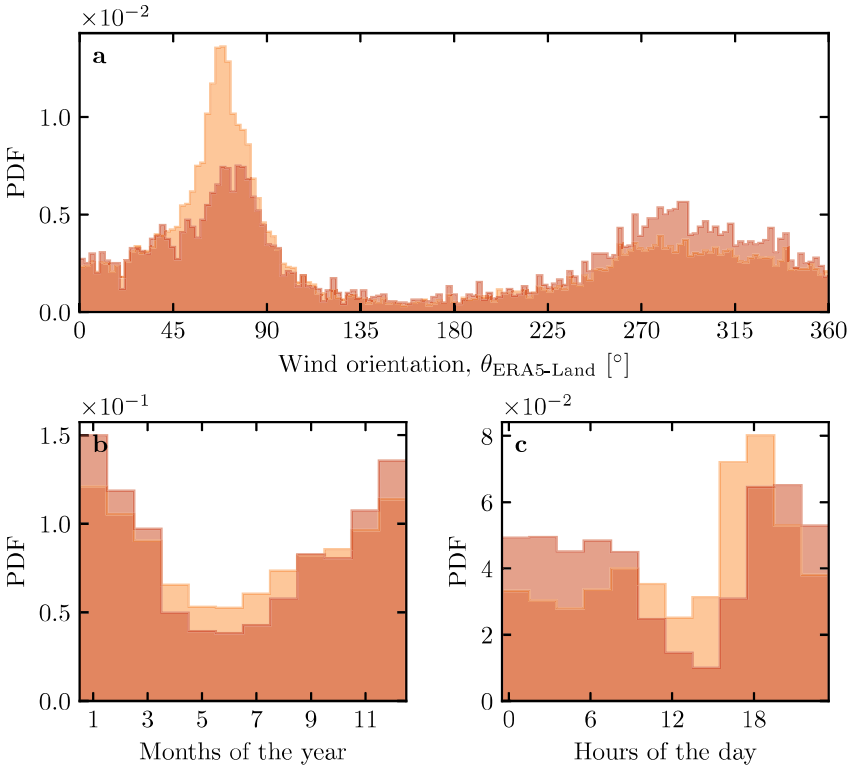

Fig. S12 Normalized distributions of amplified velocities for the North sand Sea (light orange: $\delta_u < 0$, orange: $\delta_u < -0.5$). **a**: Angular distributions. **b**: Monthly distributions. **c**: Hourly distributions.

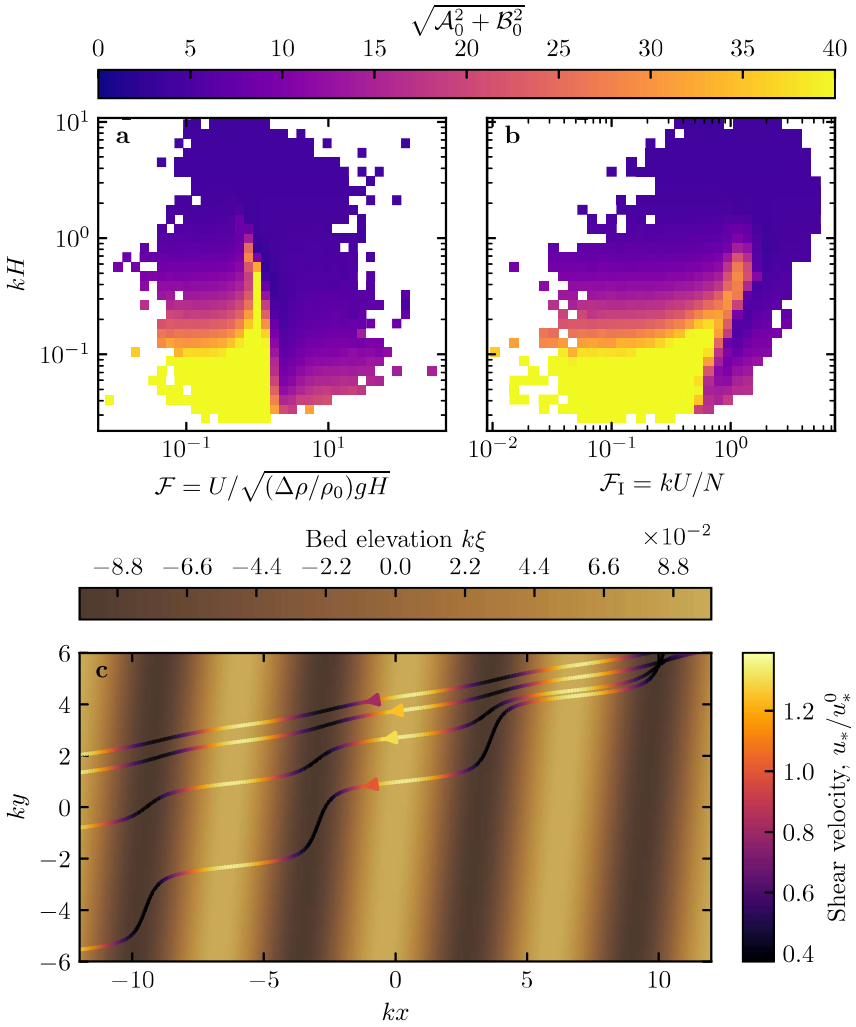

Fig. S13 Computation of the flow disturbance with the linear model of Andreotti et al. (2009). **a–b**: Magnitude of the hydrodynamic coefficients $\mathcal{A}_0$ and $\mathcal{B}_0$, calculated from the time series of the non-dimensional numbers corresponding to the ERA5-Land wind data and ERA5 data on vertical pressure levels. **c** Shear velocity streamlines over sinusoidal ridges of amplitude $k\xi_0 = 0.1$ and for increasing values of $\sqrt{\mathcal{A}_0^2+\mathcal{B}_0^2}$. From the upper to the lower streamline, values of $\left(kH,\ \mathcal{F},\ \mathcal{F}_\mathrm{I},\ \mathcal{A}_0,\ \mathcal{B}_0,\ \sqrt{\mathcal{A}_0^2+\mathcal{B}_0^2}\right)$ are (1.9, 0.6, 1.5, 3.4, 1.0, 3.5), (1.5, 0.3, 0.4, 4.8, 1.4, 5.0), (0.1, 3.5, 1.0, 8.6, 0.1, 8.6), (0.5, 0.05, 0.04, 9.6, 2.5, 9.9).

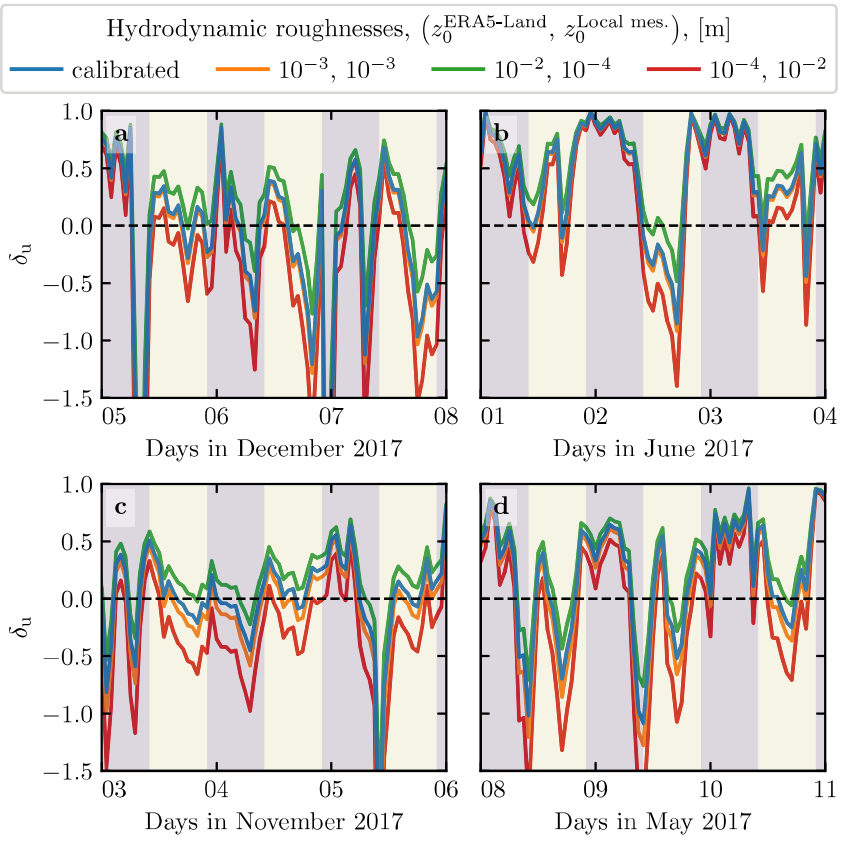

Fig. S14 Time series of the relative velocity disturbance δ_u corresponding to Fig. 5, for different values of the hydrodynamic roughnesses. **a**: North Sand Sea – summer, **b**: North Sand Sea – winter, **d**: South Sand Sea – summer, **e**: South Sand Sea – winter. Note that δ_θ is independent of the choice of $z_0^{\text{ERA5-Land}}$ and $z_0^{\text{Local mes.}}$.